

An adaptive lattice Boltzmann method for predicting wake fields behind wind turbines

Ralf Deiterding and Stephen L. Wood

Abstract The crucial components of a dynamically adaptive, parallel lattice Boltzmann method are described. By utilizing a level set approach for geometry embedding the method can handle rotating and moving structures effectively. The approach is validated for the canonical six degrees of freedom test case of a hinged wing. Subsequently, the wake field in an array of three Vestas V27 wind turbines at prescribed rotation rate and under constant inflow condition is simulated for two different scenarios. The results show that the low dissipation properties of the lattice Boltzmann scheme in combination with dynamic mesh adaptation are able to predict well-resolved vortex structures far downstream at moderate computational costs.

1 Introduction

The rotor of a horizontal axis wind turbine creates a significant wake field in the downstream wind direction. When multiple wind turbines are placed in an array, the question of optimal placement arises. If a turbine is exposed to a major vortex field, its energy output will generally be reduced and additionally induced structural vibrations will cause disproportionately accelerated material fatigue. In order to simulate the flow field in a turbine array layout, e.g., for a dominant wind direction, vortex or disc actuator models are presently most frequently adopted. Computational fluid dynamics (CFD) with accurate consideration of the moving structures is still rarely applied, which is due to the complexities involved in solving the weakly or incom-

Ralf Deiterding
Aerodynamics and Flight Mechanics Research Group, University of Southampton, Highfield Campus, Southampton SO17 1BJ, United Kingdom, e-mail: r.deiterding@soton.ac.uk

Stephen L. Wood
University of Tennessee - Knoxville
The Bredesen Center, Knoxville, TN 37996, USA e-mail: swood@utk.edu

pressible Navier-Stokes equations on moving three-dimensional meshes effectively, cf. [11].

As an alternative to the implicit, typically pressure-correction based CFD solution algorithms generally applied in wind engineering [11], we adopt in here the lattice Boltzmann method (LBM). The LBM is based on solving the Boltzmann equation in a specially chosen, discrete phase space and fully explicit in time [7]. The LBM is constructed on uniform Cartesian grids and geometrically complex boundaries are considered with an immersed boundary approach, making the method well suited for considering moving structures. Here, we utilize a level set distance function to represent embedded objects. Dynamic mesh adaptation is applied in addition in order to increase the local resolution based on the level set function and features detected in the flow field [4]. Distributed memory parallelization is adopted to allow for large-scale simulations.

The paper is organized as follows: In Section 2, we recall the construction principles of the LBM and our embedded boundary treatment method. In Section 3, the block-based mesh adaptation procedure and in particular the incorporation of the LBM are presented. Section 4 explains our approach in dealing with embedded geometries. Section 5 discusses a first validation configuration of a hinged wing and Section 6 presents first simulations of entire wind turbines that demonstrate the benefit of the proposed overall approach. The conclusions are given in Section 7.

2 Lattice Boltzmann method

The lattice Boltzmann method is based on computing approximations of the Boltzmann equation with a simplified collision operator

$$\partial_t f + \mathbf{u} \cdot \nabla f = \omega(f^{eq} - f) \quad (1)$$

on a rectangular grid of characteristic domain length L with isotropic mesh spacing Δx under the assumption of a small Knudsen number $\text{Kn} = l_f/L \ll 1$, where the mean free path length l_f is replaced with Δx . A crucial idea of the LBM is to approximate Eq. (1) in a specially chosen discrete phase space, in which a partial density distribution function $f_\alpha(\mathbf{x}, t)$ is associated to every discrete lattice velocity \mathbf{e}_α . The total density distribution is given as $\rho(\mathbf{x}, t) = \sum_\alpha f_\alpha(\mathbf{x}, t)$ and the macroscopic moments as $\rho(\mathbf{x}, t)u_i(\mathbf{x}, t) = \sum_\alpha \mathbf{e}_{\alpha i} f_\alpha(\mathbf{x}, t)$. A splitting approach is then adopted that first solves the homogeneous transport equation with the time-explicit update step

$$\mathcal{T} : \quad \tilde{f}_\alpha(\mathbf{x} + \mathbf{e}_\alpha \Delta t, t + \Delta t) = f_\alpha(\mathbf{x}, t). \quad (2)$$

Here, we apply the D3Q19 model for which the lattice velocities are defined as

$$\mathbf{e}_\alpha = \begin{cases} 0, & \alpha = 0, \\ (\pm 1, 0, 0)c, (0, \pm 1, 0)c, (0, 0, \pm 1)c, & \alpha = 1, \dots, 6, \\ (\pm 1, \pm 1, 0)c, (\pm 1, 0, \pm 1)c, (0, \pm 1, \pm 1)c, & \alpha = 7, \dots, 18, \end{cases}$$

with $c = \Delta x / \Delta t$. The physical speed of sound c_s is related to c by $c_s = c / \sqrt{3}$. The right-hand of Eq. (1) is integrated subsequently by the collision operator

$$\mathcal{C} : f_\alpha(\cdot, t + \Delta t) = \tilde{f}_\alpha(\cdot, t + \Delta t) + \omega_L \Delta t (\tilde{f}_\alpha^{eq}(\cdot, t + \Delta t) - \tilde{f}_\alpha(\cdot, t + \Delta t)) \quad (3)$$

with equilibrium function

$$f_\alpha^{eq}(\rho, \mathbf{u}) = \rho t_\alpha \left[1 + \frac{3\mathbf{e}_\alpha \mathbf{u}}{c^2} + \frac{9(\mathbf{e}_\alpha \mathbf{u})^2}{2c^4} - \frac{3\mathbf{u}^2}{2c^2} \right] \quad (4)$$

with $t_0 = 1/3$, $t_\alpha = 1/18$ for $\alpha = 1, \dots, 6$ and $t = 1/36$ for $\alpha = 7, \dots, 18$. The hydrodynamic pressure for the equilibrium function (4) reads $p = \sum_\alpha f_\alpha^{eq} c_s^2 = \rho c_s^2$.

Applying a Chapman-Enskog expansion procedure, it can be shown [8] that the sketched LBM converges to a solution of the weakly compressible Navier-Stokes equations

$$\partial_t \rho + \nabla \cdot (\rho \mathbf{u}) = 0, \quad (5a)$$

$$\partial_t \mathbf{u} + \mathbf{u} \cdot \nabla \mathbf{u} = -\nabla p + \nu \nabla^2 \mathbf{u}. \quad (5b)$$

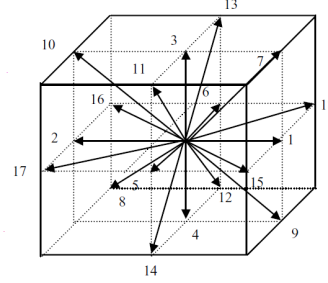


Fig. 1 The velocities \mathbf{e}_α of the D3Q19 lattice.

It can be shown further, cf. [7], that the kinematic viscosity ν and the collision frequency of the LBM, ω_L , are connected by the relation

$$\omega_L = \tau_L^{-1} = \frac{c_s^2}{\nu + \Delta t c_s^2 / 2}. \quad (6)$$

While the sketched model can be used directly to simulate laminar flows, it is mandatory to apply a turbulence model in addition in high Reynolds number situations. In the context of LBM, it is common to adopt a large eddy simulation approach and assume that the partial density distribution functions used in the scheme represent the resolved scales. The subgrid scale turbulence is then considered by adding a turbulent viscosity ν_t to the physical one and utilize the effective viscosity $\nu^* = \nu + \nu_t = \frac{1}{3} \left(\frac{\tau_L^*}{\Delta t} - \frac{1}{2} \right) c \Delta x$ with $\tau_L^* = \tau_L + \tau_t =: 1/\omega_L^*$ in (3) throughout the scheme. Like Hou *et al.* [8], we apply the Smagorinsky model to evaluate ν_t , for which $\nu_t = (C_{sm} \Delta x)^2 \bar{S}$, where we use $C_{sm} = 0.2$ here, with

$$\bar{S} = \sqrt{2 \sum_{i,j} \bar{S}_{ij} \bar{S}_{ij}}, \quad \bar{S}_{ij} = \frac{\Sigma_{ij}}{2\rho_0 c_s^2 \tau_L^* \left(1 - \frac{\omega_L \Delta t}{2} \right)} = \frac{1}{2\rho_0 c_s^2 \tau_L^*} \sum_\alpha \mathbf{e}_{\alpha i} \mathbf{e}_{\alpha j} (\tilde{f}_\alpha^{eq} - \tilde{f}_\alpha), \quad (7)$$

where Σ_{ij} denotes the deviatoric stress tensor. From (7) one ultimately obtains [8]

$$\tau_t = \frac{1}{2} \left(\sqrt{\tau_L^2 + 18\sqrt{2}(\rho_0 c^2)^{-1} C_{sm}^2 \Delta x \bar{S}} - \tau_L \right). \quad (8)$$

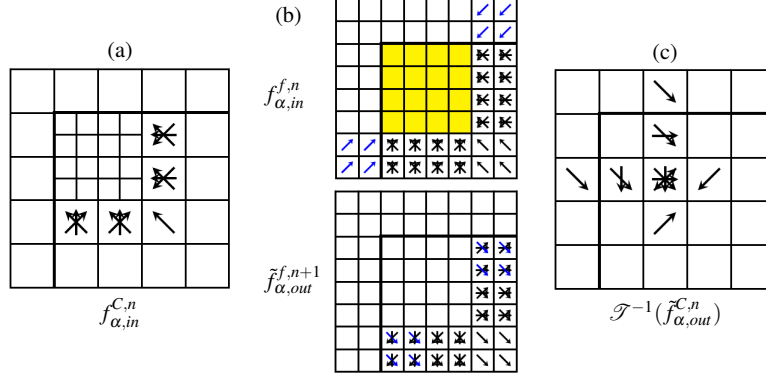


Fig. 2 Visualization of distributions involved in necessary data exchange at a coarse-fine boundary. The thick black lines indicate a physical boundary. (a) Coarse distributions going into fine grid; (b) ingoing interpolated fine distributions in halos (top), outgoing distributions in halos after two fine-level transport steps (bottom); (c) averaged distributions replacing coarse values before update is repeated in cells next to boundary.

3 Dynamic mesh adaptation

For local dynamic mesh adaptation we have adopted the block-structured adaptive mesh refinement (SAMR) method after Berger & Collela [1]. In order to fit smoothly into our existing, fully parallelized finite volume SAMR software system AMROC [4], we have implemented the LBM cell-based, which makes the scheme also conservative in ρ and ρu_i . In the SAMR approach, finite volume cells are clustered with a special algorithm into non-overlapping rectangular grids. The grids have a suitable layer of halo cells for synchronization and applying inter-level and physical boundary conditions. Refinement levels are integrated recursively. The spatial mesh width Δx_l and the time step Δt_l are refined by the same factor r_l , where we assume $r_l \geq 2$ for $l > 0$ and $r_0 = 1$. Note that in an adaptive LBM the collision frequency ω_L is not a constant but needs to be adjusted according to Eq. (6) for the update on each level. In addition to this, the interface region requires a specialized treatment. Distinguishing between the transport and collision operators, \mathcal{T} and \mathcal{C} , cf. Eqs. (2) and (3), the crucial steps of our method are:

1. Use coarse grid distributions $f_{\alpha,in}^{C,n}$ that propagate into the fine grid, cf. Fig. 2a, to construct initial fine grid halo values $f_{\alpha,in}^{f,n}$, cf. Fig. 2b, by interpolation.
2. Transport $\tilde{f}_{\alpha}^{f,n} := \mathcal{T}(f_{\alpha}^{f,n})$ on entire fine mesh. Collision $f_{\alpha}^{f,n+1/2} := \mathcal{C}(\tilde{f}_{\alpha}^{f,n})$ is applied only in the interior cells (yellow in Fig. 2b). Repeat $r_l - 1$ times.
3. Average outgoing distributions from fine grid halos (Fig. 2c) to obtain $\tilde{f}_{\alpha,out}^{C,n}$.
4. Reverse transport for averaged outgoing distributions, $\tilde{f}_{\alpha,out}^{C,n} := \mathcal{T}^{-1}(\tilde{f}_{\alpha,out}^{C,n})$, and overwrite those in the previous coarse grid time step, cf. Fig. 2d.
5. Repeat LBM update on coarse grid cells next to coarse-fine boundary only.

This algorithm is computationally equivalent to the method by Chen *et al.* [2] but tailored to the SAMR recursion that updates coarse grids in their entirety before fine grids are computed. Because of the nonlinearity of the collision operator \mathcal{C} it becomes necessary under this paradigm to repeat the LBM update for those coarse grid cells that share a face or corner with a fine grid.

4 Embedded structure handling

We represent non-Cartesian boundaries implicitly on the adaptive Cartesian grid by utilizing a scalar level set function φ that stores the distance to the boundary surface. The boundary surface is located exactly at $\varphi = 0$ and the boundary outer normal in every mesh point can be evaluated as $\mathbf{n} = -\nabla\varphi/|\nabla\varphi|$ [3]. We treat a fluid cell as an embedded ghost cell if its *midpoint* satisfies $\varphi < 0$.

In order to implement non-Cartesian boundary conditions with the LBM, we have chosen to pursue a 1st order accurate ghost fluid approach that was already available in AMROC [3]. In our technique, the density distributions in embedded ghost cells are adjusted to model the boundary conditions of a non-Cartesian reflective wall moving with velocity \mathbf{w} before applying the unaltered LBM. The last step involves interpolation and mirroring of ρ , \mathbf{u} across the boundary to ρ' and $\bar{\mathbf{u}}$ and modification of the macro velocity in the immersed boundary cells to $\mathbf{u}' = 2\mathbf{w} - \bar{\mathbf{u}}$, cf. [4]. From the newly constructed macroscopic values the density distributions in the embedded ghost cells are simply set to $f_{\alpha}^{eq}(\rho', \mathbf{u}')$.

Real-world geometries are considered in AMROC as triangular surface meshes. The computation of the level set distance information in every Cartesian cell midpoint could principally be accomplished by simply iterating over the entire surface mesh; yet, this would lead to detrimental performance for increasing problem size. Instead, we employ a specially developed algorithm based on characteristic reconstruction and scan conversion by Mauch [10] that is used to compute the distance exactly only in a small band around the embedded structure.

The dynamics of multi-body systems undergoing interaction with the fluid are modeled as sets of triangulated surface meshes configured in kinetic chains. The dynamics of these mechanisms are solved by a recursive Newton-Euler method at each time step [13]. Considering an arbitrary link with a coordinate frame located at point \mathbf{P} that is not coincident with its associated body's center of mass, the force and torque applied by the preceding link are

$$\begin{pmatrix} \mathbf{F} \\ \boldsymbol{\tau}_P \end{pmatrix} = \begin{pmatrix} m\mathbf{1} & -m[\mathbf{c}]^{\times} \\ m[\mathbf{c}]^{\times}\mathbf{I}_{cm} & -m[\mathbf{c}]^{\times}[\mathbf{c}]^{\times} \end{pmatrix} \begin{pmatrix} \mathbf{a}_P \\ \boldsymbol{\alpha} \end{pmatrix} + \begin{pmatrix} m[\boldsymbol{\omega}]^{\times}[\boldsymbol{\omega}]^{\times}\mathbf{c} \\ [\boldsymbol{\omega}]^{\times}(\mathbf{I}_{cm} - m[\mathbf{c}]^{\times}[\mathbf{c}]^{\times})\boldsymbol{\omega} \end{pmatrix}. \quad (9)$$

Here, we additionally define the total force and torque acting on a body, $\mathbf{F} = (\mathbf{F}_{FSI} + \mathbf{F}_{prescribed}) \cdot \mathcal{C}_{xyz}$ and $\boldsymbol{\tau} = (\boldsymbol{\tau}_{FSI} + \boldsymbol{\tau}_{prescribed}) \cdot \mathcal{C}_{\alpha\beta\gamma}$ respectively. Where \mathcal{C}_{xyz} and $\mathcal{C}_{\alpha\beta\gamma}$ are the translational and rotational constraints, respectively. \mathbf{F}_{FSI} and $\boldsymbol{\tau}_{FSI}$ are determined for each body by integrating the fluid pressure on the triangular facets of

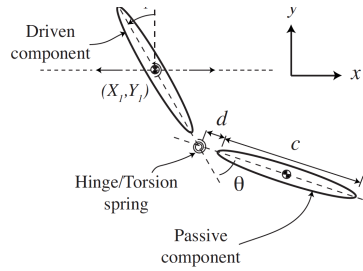


Fig. 3 Model system consisting of two rigid elliptical sections connected by a hinge with torsion spring and damper.

Table 1 Kinematic parameters

A_0 (cm)	7.1
c (cm)	5.1
d (cm)	0.25
β	$\pi/4$
σ_t	0.628
σ_r	0.628
Φ	0
Re_t	73, 370
Re_r	100, 500
ρ_b (kg/m ³)	5080
f (Hz)	0.15

the respective body's surface mesh. Each surface mesh is associated with a kinetic link in a chain that begins with a base link in the global coordinate frame. Links are connected by joints that may be independently constrained in six degrees of freedom relative to the preceding link. The evolution of the triangular surface mesh as well as the velocity \mathbf{w} in each node are communicated to the LBM fluid solver in dedicated coupling time steps. The data exchange corresponds to the time step of an SAMR level but this does not have to be the finest refinement level available, cf. [5].

5 Fluid-structure interaction verification

A canonical problem of fluid-structure interaction and wake prediction proposed by Toomey & Eldredge [12] is selected for verification. This model, depicted in Fig. 3, utilizes a system of two articulated rigid bodies connected by a torsion spring and damper. The kinematics of the centroid of the driven wing are prescribed, while the trailing body responds passively to the aerodynamic and inertial/elastic forces. The principle unknown in this rigid body dynamics problem is the hinge angle θ . The set of parametric kinematic equations (1)-(5) in [12] describe the motion of the driven body. The parameters utilized in this work and in Case 1 of [12] to specify the kinematics are given in Table 1. The mean and peak values of the dimensionless fluid dynamic force, $F_{x,y} = 2F_{x,y}^*/(\rho_f^2 c^3)$, and moment, $M = 2M^*/(\rho_f f^2 c^4)$, generated by the wing motion are presented in Table 2 for the rotational Reynolds numbers $Re_r = 2\pi\beta\sigma_r f c^2 / (\tanh(\sigma_r)\nu) = \{100, 500\}$. The relative error between the results of this work and the computational results in [12] evaluated over three periods of motion is presented in Table 2. The used spatial resolution in [12] was $\Delta x/c = 0.013$ and $\Delta x/c = 0.0032$ for $Re_r = 100$ and 500, respectively, while we have used an adaptive mesh with up to three additional levels with finest spatial resolution around the structure of $\Delta x/c = 0.0122$ for both cases. Due to the time-explicit nature of the LBM, our finest temporal resolution is respectively ~ 113 and ~ 28 higher than in the computations in [12]. The good quantitative agreement of the LBM-based predictions with those from the viscous vortex particle method adopted in [12] provides verification for our fluid-structure coupling methodology.

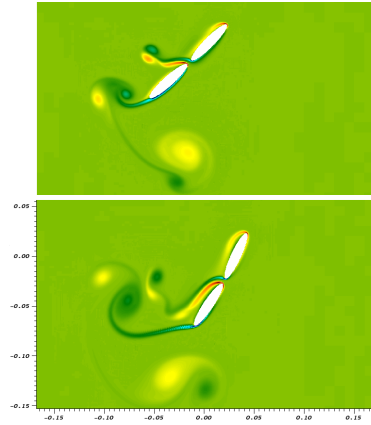


Table 2 Nondimensional mean and peak force and moments

	$Re_r = 100$		$Re_r = 500$	
	Mean	Peak	Mean	Peak
F_x	2.63	498.0	3.77	498.0
ΔF_x (%)	-2.59	4.4	-3.4	4.4
F_y	31.0	228.0	58.0	235.0
ΔF_y (%)	3.33	5.07	5.45	3.98
M	-2.50	184.0	0.77	184.0
ΔM (%)	-3.85	-3.66	-3.75	-4.17

Fig. 4 Left: Computed vorticity field at $t/T=0.6$, 0.8 for $Re_r = 500$

Our simulation results of wing deflection and vorticity production at $Re_r = 500$ are depicted in Fig. 4. Figure 5 displays the hinge deflection angle predicted by this simulation over three periods versus the experimental result from [12]. Note that the rotational Reynolds number in the experiment is slightly larger with $Re_r = 2200$, while the values 100 and 500 were chosen in [6, 12] to reduce the required spatial resolution. Nevertheless, wing behavior and computationally predicted loads are well comparable to the experiment, providing validation for our approach.

6 Simulation of wakes behind wind turbines

Utilizing the developed LBM solver for moving geometries, we have carried out a simulation campaign to test the suitability of the overall approach to simulate the flow fields created by wind turbines. We have built a tailored flexible surface mesh model of a Vestas V27 turbine. The V27 has a rotor diameter of $D = 27$ m, a tower height of ~ 35 m and achieves its maximal energy output of 225 kW at wind velocities from 14 to 25 m/s. A prototypical ground topology is also included into the surface mesh model that represents the time-dependent geometry with $\sim 23,300$ facets per turbine. It is assumed that the inflow wind direction is always in direction of the turbine middle axis and the pitch blade angle is at 0 degree.

Figure 6 shows a snapshot from a first test simulation with three additional levels refined by the factors $r_{1,2} = 2$ and $r_3 = 4$. Displayed are the Cartesian cells in the rotor midplane and the moving structure colored by the length of the prescribed velocity vector, which illustrates how the mesh is following the rotating structure. The effective resolution around rotor and tower is $\Delta x = 3.125$ cm.

The setup investigated more in depth considers three V27 turbines and corresponds to the U.S. Department of Energy’s Scaled Wind Farm Technology (SWIFT) facility. Two turbines are positioned $3D$ apart in the wind direction; the third turbine is placed $5D$ downstream exactly in the rotor middle axis of the first one. The

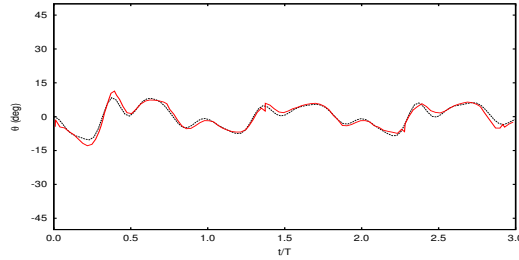


Fig. 5 Hinge deflection angle over time. Experimental results (—); Current (---).

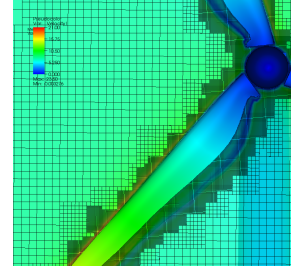


Fig. 6 Snapshot of SAMR Mesh in rotor midplane.

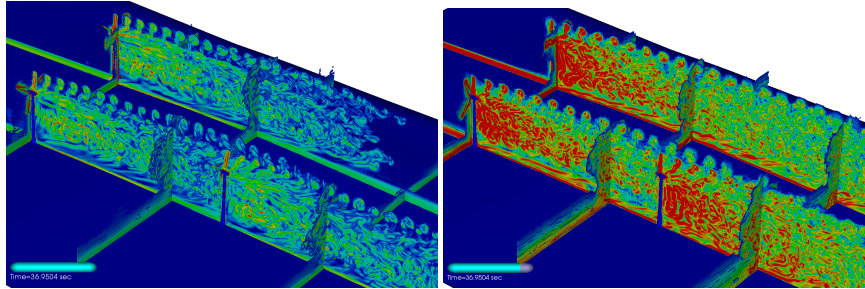


Fig. 7 2D Color planes depict the length of the vorticity vector for 7 m/s (left) and 25 m/s (right) inflow velocity. Simulated physical time is $t \approx 37$ s.

tower center lines are perpendicular to the xy -plane and their locations are $(0,0)$, $(135\text{ m},0)$, and $(-5.65\text{ m},80.80\text{ m})$. For wind in the x -direction, this setup allows direct comparison of the wake fields created by two interacting turbines and a single, isolated turbine. Our computations use a domain of $448\text{ m} \times 240\text{ m} \times 100\text{ m}$, which is discretized with a base resolution of $448 \times 240 \times 100$ cells and refined isotropically by the factors 2,2,4 (resolution near the rotors is $\Delta x = 6.25\text{ cm}$). Dynamic refinement of the wake field is permitted up to level 2, yielding a resolution in the wake of $\Delta x = 25\text{ cm}$.

Two simulations have been carried out: a case with $u_1 = 7\text{ m/s}$ inflow velocity and all turbines operating at 15 rpm and a simulation with $u_1 = 25\text{ m/s}$ and 43 rpm, which corresponds to the maximal rotation rate under normal operations. 94,224 highest level iterations to a time of $t = 40\text{ s}$ were computed. Figure 7 depicts the wake fields for both cases after $t \approx 37\text{ s}$ simulated time. The color coding in both graphics uses the same scale and it is apparent that vorticity production is considerably increased in the second configuration. In both simulations, the diameter of the main vortex systems are only slightly increasing. Overall, vorticity seems well preserved and a strong influence of the tower on the wake field can be seen. The difference between the single- and the two-turbine wake is striking.

A quantitative analysis of characteristic flow field statistics is provided for the case $u_1 = 25\text{ m/s}$ and 43 rpm. This simulation is continued for another 23,555 iter-

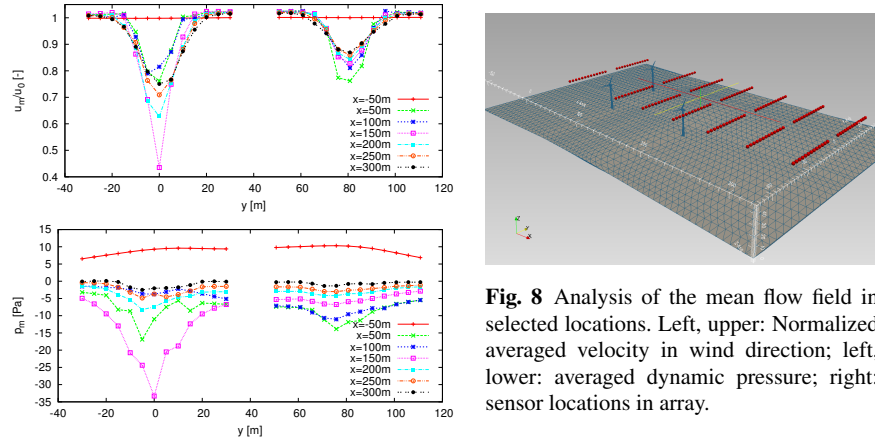


Fig. 8 Analysis of the mean flow field in selected locations. Left, upper: Normalized averaged velocity in wind direction; left, lower: averaged dynamic pressure; right: sensor locations in array.

ations for the interval $[40s, 50s]$ to compute time-averaged values in selected point locations arranged in lines 50 m apart at $z = 37$ m. The sensor positions are indicated by the red spheres in the right graphic of Fig. 8. The left graphics depict the deficit in the normalized mean velocity component in the x -direction and the mean dynamic pressure due to the presence of the turbines. The introduction of an additional velocity deficit by the second turbine that is decreasing with increasing downstream distance can be clearly inferred. On the other hand, an increase in average pressure in front of the second turbine (at $x = 100$ m) is also visible.

The used SAMR grids and total number of cells on each level for this simulation at $t = 40$ s are given in Table 3. Note that a corresponding uniform mesh would require $44 \cdot 10^9$ cells and take four times more time steps than level 2, which contains the majority of cells. The computation of the statistics interval from $t = 40$ s to $t = 50$ s on 288 cores on a cluster of Intel-Ivybridge CPUs required just 38.5 h wall clock time (11,090 h CPU), which gives evidence for the practical feasibility of carrying out these computations on compute clusters of moderate size.

Level	Grids	Cells
0	3,234	10,752,000
1	11,921	21,020,256
2	66,974	102,918,568
3	896	5,116,992

Table 3 Grids and cells at t_e .

7 Conclusions

The prototype of a dynamically adaptive, three-dimensional lattice-Boltzmann method for simulating the wake fields behind realistic, rotating wind turbines has been developed. First validation has been achieved for a canonical FSI problem from [12]. We have confirmed that our approach is able to simulate the propagation of wake fields created by the rotation of accurate Vestas V27 wind turbine rotor geometry, including the interaction with the tower, with apparent good quality and comparably moderate computational costs.

Immediate future work will concentrate on validating the approach for available laboratory benchmarks, e.g., the Mexico wind tunnel experiments [11] and then to consider the dynamic elastic response of the blades in the turbine model. Further on, it is planned to incorporate enhanced wall-near treatment approaches into the LBM for turbulent flows. For cases that fully resolve turbulent boundary layers, the damping of the Smagorinsky constant by the van Driest approach can be easily implemented, cf. [14]; for high Reynolds number situations, in which accurate resolution of the boundary layer is prohibitively expensive with a Cartesian method, a wall function model will be implemented. The consistent integration of a wall function model into the LBM with Smagorinsky large-eddy simulation approach has been demonstrated by Malaspinas & Sagaut [9].

Acknowledgements Stephen L. Wood was supported by the TN-SCORE Energy Scholar program funded by NSF EPS-1004083 during this work.

References

1. Berger, M., Colella, P.: Local adaptive mesh refinement for shock hydrodynamics. *J. Comput. Phys.* **82**, 64–84 (1988)
2. Chen, H., Filippova, O., Hoch, J., Molvig, K., Shock, R., Teixeira, C., Zhang, R.: Grid refinement in lattice Boltzmann methods based on volumetric formulation. *Physica A* **362**, 158–167 (2006)
3. Deiterding, R.: A parallel adaptive method for simulating shock-induced combustion with detailed chemical kinetics in complex domains. *Computers & Structures* **87**, 769–783 (2009)
4. Deiterding, R.: Block-structured adaptive mesh refinement - theory, implementation and application. *European Series in Applied and Industrial Mathematics: Proceedings* **34**, 97–150 (2011)
5. Deiterding, R., Wood, S.L.: Parallel adaptive fluid-structure interaction simulations of explosions impacting building structures. *Computers & Fluids* **88**, 719–729 (2013)
6. Eldredge, J.D., Toomey, J., Medina, A.: On the roles of chord-wise flexibility in a flapping wing with hovering kinematics. *Journal of Fluid Mechanics* **659**, 94–115 (2010)
7. Hähnel, D.: *Molekulare Gasdynamik*. Springer (2004)
8. Hou, S., Sterling, J., Chen, S., Doolen, G.D.: A lattice Boltzmann subgrid model for high Reynolds number flows. In: A.T. Lawniczak, R. Kapral (eds.) *Pattern formation and lattice gas automata*, vol. 6, pp. 151–166. *Fields Inst Comm* (1996)
9. Malaspinas, O., Sagaut, P.: Wall model for the large-eddy simulation based on the lattice Boltzmann method. *J. Comput. Phys.* **275**, 25–40 (2014)
10. Mauch, S.P.: Efficient algorithms for solving static hamilton-jacobi equations. Ph.D. thesis, California Institute of Technology (2003)
11. Schepers, J.G., Boorsma, K.: Final report of iea task 29: Mexnext (phase 1) – Analysis of Mexico wind tunnel measurements. *Tech. Rep. ECN-E-12-004*, European research Centre of the Netherlands (2012)
12. Toomey, J., Eldredge, J.D.: Numerical and experimental study of the fluid dynamics of a flapping wing with low order flexibility. *Physics of Fluids (1994-present)* **20**(7), 073603 (2008)
13. Tsai, L.: *Robot Analysis: The Mechanics of Serial and Parallel Manipulators*. Wiley (1999)
14. Weickert, M., Teike, G., Schmidt, O., Sommerfeld, M.: Investigation of the LES WALE turbulence model within the lattice Boltzmann framework. *Comput. Math. Appl.* **59**, 2200–2214 (2010)